WILEY
Aggregate Open Access

RESEARCH ARTICLE OPEN ACCESS

Enantioselective Lanthanide Binding Modulates Collagen Self-Assembly

Radek Pelc[1,2] | Jiří Kessler[1] | Jaroslav Šebestík[1] | Martin Šafařík[1] | Petr Bouř[1] | Tao Wu[1]

[1]Institute of Organic Chemistry and Biochemistry, Czech Academy of Sciences, Prague, Czech Republic | [2]Third Faculty of Medicine, Charles University, Prague, Czech Republic

Correspondence: Tao Wu (tao.wu@uochb.cas.cz)

Received: 21 November 2025 | **Revised:** 23 January 2026 | **Accepted:** 30 January 2026

Keywords: circularly polarized luminescence | collagen aggregation | connective tissue | fibrillogenesis | molecular dynamics | Raman microscopy

ABSTRACT

Collagen fibrillogenesis underlies the structural and mechanical properties of the extracellular matrix in connective and other tissues, yet its molecular mechanism remains poorly understood. Here, we show that a europium(III) dipicolinate complex (EuDPA) acts as a luminescent reporter of collagen aggregation. We combine Raman microscopy, circularly polarized luminescence (CPL), and molecular dynamics (MD) simulations to study this process. While Raman imaging directly visualizes the EuDPA-enhanced fibrillar architecture, CPL reveals enantioselective EuDPA–collagen interactions that accompany the fibrillogenesis. MD simulations indicate the presence of stabilizing interactions between hydroxyproline residues and the dipicolinate ligand. The results pave the way to monitoring of protein aggregation in general, and are relevant to fibrotic pathologies and biomimetic materials design.

1 | Introduction

Collagen is the main component of the connective tissue found in tendons, skin, cartilage, and bone. Its fibril-forming types (I, II, III, V, and XI) are the most significant species, and are involved in aging and many pathophysiological processes such as cystic fibrosis or cancer. Their highly ordered packing and hierarchical bundling not only underlie collagen's mechanical resilience in vivo but also translate to its long-term stability in archaeological findings [1].

A well-known structural feature of collagen is its triple helix, in which three polypeptide chains adopt a polyproline II-type (PPII) conformation stabilized by intramolecular hydrogen bonding. The most common amino acids in it are proline (Pro, P), hydroxyproline (Hyp, H), and glycine (Gly, G). The ProHypGly (PHG) triplet is fundamental in assembling the helical chains [2]. Although atomic-level features have been extensively studied since the 1950s [3–6], many aspects of collagen fibrillogenesis remain incompletely understood [7]. Even the most advanced biomolecule-structure prediction algorithms, such as AlphaFold2 [8] and AlphaFold3 [9], struggle to describe higher-order collagen assemblies.

Conventional methods such as X-ray crystallography, scanning electron microscopy (SEM) [10], and mass spectroscopy (MS) [11] can provide valuable structural information, but are inherently limited to studying only in dry state. The atomic force microscope (AFM) of collagen can handle hydrated specimens [7], and optical methods also represent a suitable alternative. For example, second-harmonic generation (SHG) microscopy enables label-free visualization of fibrillar collagen in intact tissues [12, 13], while vibrational (Raman in particular) spectroscopy [14–16] offers a label-free, non-destructive way to characterize collagen conformation in hydrated specimens [16]. Raman imaging of protein-specific modes, such as amide

vibrations, poses significant challenges because the signal is weak compared to that of the dominant C—H stretching [17, 18], especially when lipids are present in the specimen.

Lanthanide probes are frequently used to study photophysical properties of molecules, including their sensitivity to local chiral environment [19–21]. Lanthanide-binding proteins/peptides may help to elucidate the structure and function of living systems, and thus far have been investigated by X-ray crystallography, fluorescence spectroscopy, and NMR spectroscopy [22–24]. Among them, Eu(III) complexes appear particularly suitable for chemical imaging because the relevant transition ($^5D_0 \rightarrow {}^7F_2$) at ~615 nm does not overlap with vibrational Raman bands if the standard 532 nm excitation is used. This makes it possible to simultaneously record luminescence and Raman signal. Chiral-contrast imaging is yet another promising application [25].

Chiroptical spectroscopies (e.g., circularly polarized luminescence, CPL) are indispensable to study intermolecular interactions [26, 27]. In particular, CPL detection within Raman optical activity (ROA) spectroscopy [28–31] has proven highly effective for bio-related studies, for example, in amino acids [32], peptides [33], saccharides [34], *N*-acetylneuraminic (sialic) acid [35], nucleotides [36], and DNA [37]. The lanthanide complexes prove very useful to this end, and can also be used in chemical (Raman) microscopy [38, 39]. In otherwise unstained cells, an Eu(III) complex can serve as a counterstaining agent facilitating navigation in the specimen, i.e., providing a much-needed morphological context [40].

Here we present a lanthanide-based molecular-imaging approach linking molecular chirality to higher-order fibril architecture. Specifically, we employ a europium(III) dipicolinate (EuDPA) complex acting simultaneously as a luminescent tag and a chiroptical probe. By combining Raman microscopy, ROA/CPL spectroscopy, and molecular dynamics (MD) simulations, we visualize the fibrillogenesis in collagen.

2 | Results and Discussion

2.1 | Imaging Collagen Fibrils With the Aid of a Lanthanide Raman Tag

As a label-free technique, Raman microscopy provides chemical contrast by exploiting unique vibrational fingerprints of molecules. A more refined approach employs Raman tags that provide strong spectral lines in the silent spectral range (1800–2800 cm^{-1}), where biomolecules typically do not generate measurable signals [41]. To visualize collagen fibrils, we used a water-soluble europium(III) tris(dipicolinate) complex, $Na_3[Eu(DPA)_3]$ (abbreviated as EuDPA; Figure 1) as a selective lanthanide luminescence tag. This probe binds to collagen and is readily detected through its hypersensitive Eu^{3+} emission band ($^5D_0 \rightarrow {}^7F_2$ transition at ~616 nm). This band is seen at ~2555 cm^{-1} in the Raman spectrum and is as narrow as most vibrational bands [40]. Spectral mapping of this EuDPA-specific peak revealed extended fibrillar networks that colocalized with the collagen protein C—H stretching band at ~2935 cm^{-1}. This overlap confirms the selective affinity of EuDPA for collagen and enables direct visualization of its fibrillar architecture.

Bright-field microscopy of collagen hydrogels formed in the presence of EuDPA revealed large, macroscopic fibers tens of micrometers wide (Figure 1). However, sub-micrometer details of these hydrated fibrils were not readily discernible.

When dried (Figure 2), smaller fibers/aggregates become visible, most likely because the EuDPA concentration increases during the drying process, thus facilitating fibrillogenesis. In the absence of trituration (Figure 2A–C), the EuDPA concentration considerably varies within the specimen, that is, can be locally higher (and the collagen fibers bigger) than in triturated specimens (Figure 2D). The crystal-like ordered nature of the fibers is apparent from the polarization image (Figure 2B), and colocalization of collagen I / II with EuDPA from the Raman (Figure 2C,F) and luminescence (Figure 2C,E) images. The fibers were much less numerous (or absent altogether) in control samples of collagen I / II alone and EuDPA alone (Figure 3 and Figure S3). Note that the Eu luminescence band at ~2555 cm^{-1} exhibits an intensity over two orders of magnitude higher than the strongest Raman signal of collagen I / II (the CH stretching mode at ~2935 cm^{-1}). Detailed comparison of the spectral intensities (luminescence of EuDPA vs. Raman CH-stretching band of collagen I / II) in wet and dry state are shown in Figure S4 and Figure S5, respectively.

2.2 | Modulation of Collagen Aggregation by Europium: ROA/CPL Spectroscopy

While lanthanide tagging enables direct chemical imaging of the collagen fibrils, a deeper understanding of their molecular architecture requires a chiroptical analysis. To this end, we applied a ROA-CPL detection scheme to examine how EuDPA binding affects the collagen self-assembly, as it is highly sensitive to subtle structural changes induced by the lanthanide complexes [30]. The water-soluble EuDPA complex exhibiting a pseudo-D_3 symmetry contains coordination sites capable of chelating histidine-containing peptides [42] and lysozyme [32]. Here, we employed it to investigate induced-CPL spectral responses in collagen proteins and collagen-type peptides.

EuDPA concentration below 1 mM (red traces in Figure 4A and Figure S6A), the total-luminescence ($I_R + I_L$) signal recorded at 1565 and 1546 cm^{-1} is a doublet corresponding to the $^5D_0 \rightarrow {}^7F_0$ Eu^{3+} transition (I_R and I_L denote the intensity of right- and left-circularly polarized light). This particular transition generally exhibits only a single luminescence band, and the doublet most likely indicates a competition between the two EuDPA enantiomers (Λ and Δ) for binding to collagen I. This spectral couplet gradually becomes a singlet as EuDPA concentration increases (≥2 mM).

It is interesting that collagen I (20 mg/mL) preferably binds the Λ-configuration of EuDPA [32, 42, 43] at low concentration of EuDPA (≤2 mM), and it exhibits a negative CPL ($I_R - I_L$) pattern (Figure 4B and Figure S6B), with most Raman and luminescence bands ($I_R + I_L$) remaining almost the same (Figure 4A).

As EuDPA concentration increases (≥4 mM), formation of collagen fiber(s) can be seen by the naked eye (Figure 1), and the protein starts to favor binding to the opposite (Δ) configuration of EuDPA while displaying an inverted CPL pattern. Significant

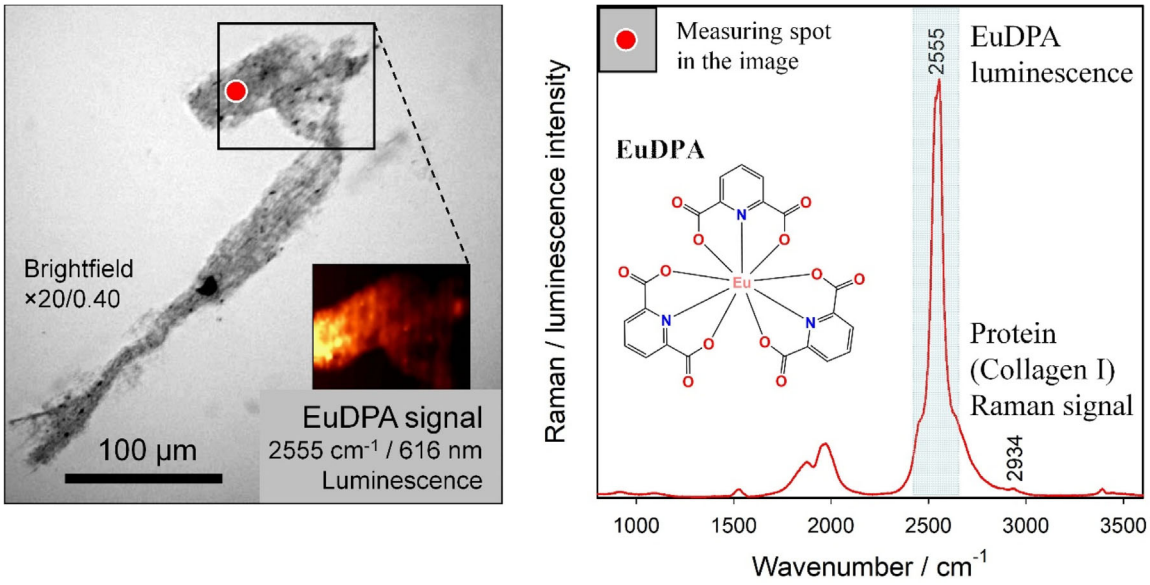

FIGURE 1 | Representative image of a protein fiber formed in wet state (solution) in a mixture of collagen I (final concentration 6.5 mg/mL) and EuDPA (final concentration 4 mM, formula in the right box). The luminescence image (inset) demonstrates colocalization of collagen and EuDPA. The spectrum comprises both the Raman and luminescence signals, and is shown at an expanded scale in Figure S4.

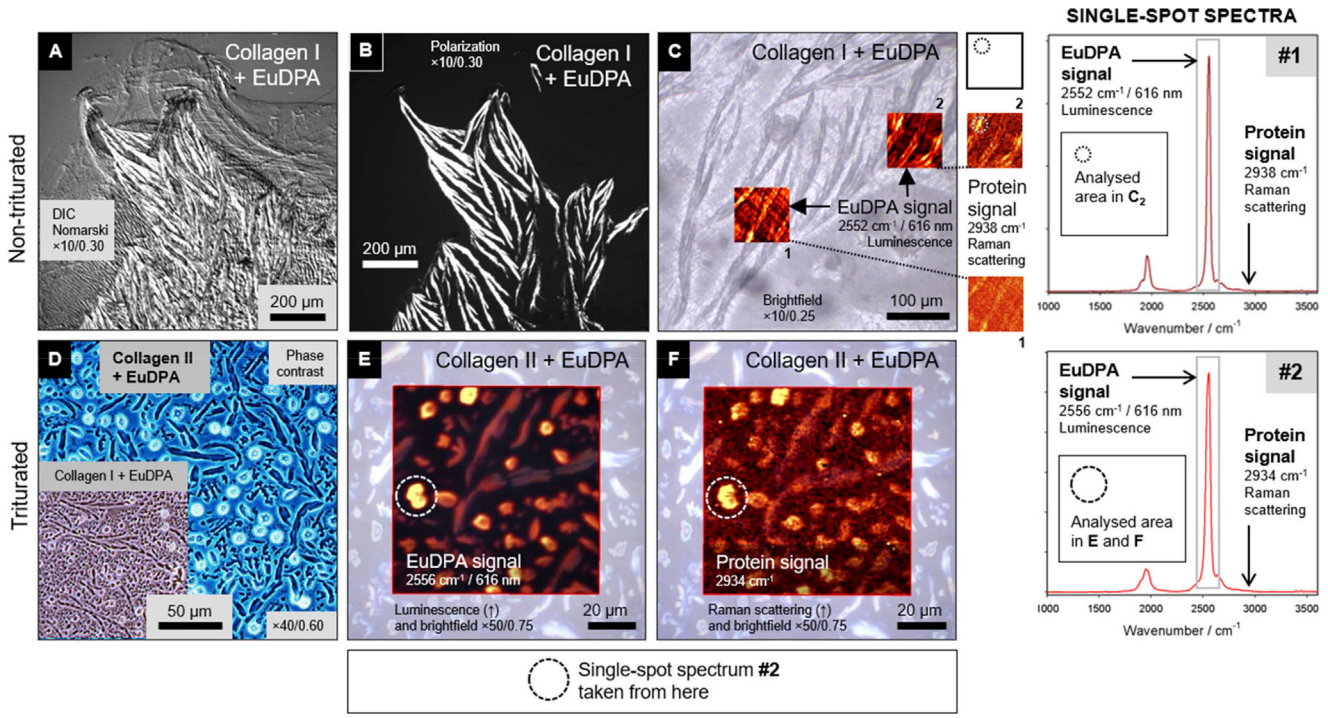

FIGURE 2 | Protein fibers/aggregates in dry state obtained by mixing collagen I or II with EuDPA (see Section 4 for details). Bigger fibers are present in non-triturated (less thoroughly mixed) samples (A-C) containing locally higher concentrations of EuDPA, and their crystalline nature is documented by the polarization image (B). Raman (C,F) and luminescence (C,E) images (shown as overlays with brightfield) reveal colocalization of collagen and EuDPA. Imaging modality and objective magnification/numerical aperture are stated for each image (DIC, differential interference contrast). A zoom-out view of A and B is shown in Figure 3. Pseudocolour rendering of the two images in D is purposely different, and their expanded versions are shown in Figure S3. Control images (collagen alone and EuDPA alone) are shown in Figure 3 and Figure S3. The spectra comprise both the Raman and luminescence signals, and are shown at an expanded scale in Figure S5.

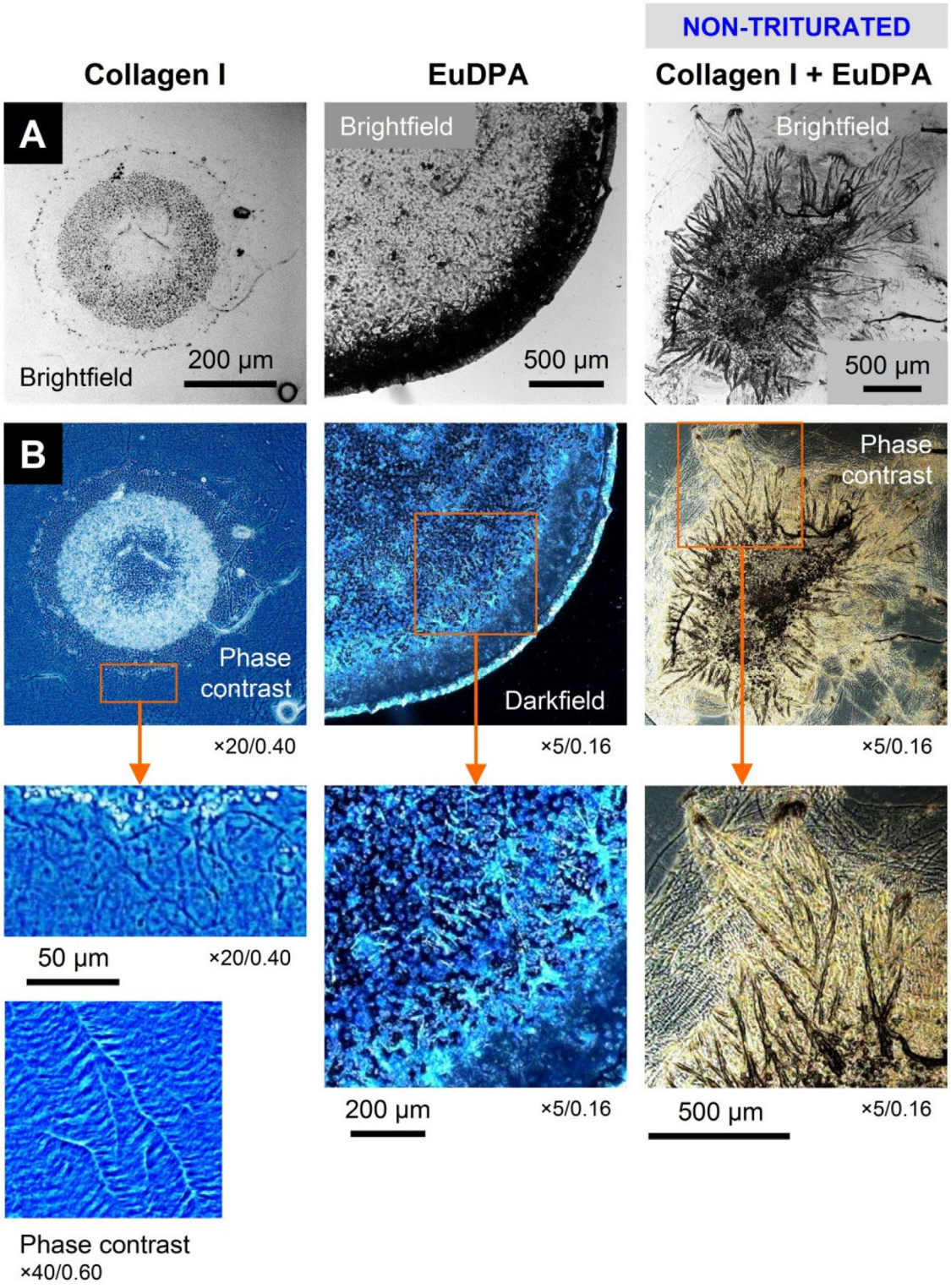

FIGURE 3 | (Right) Small-magnification overview of the "collagen + EuDPA" aggregate shown in Figure 2A,B (dry-state *non-triturated* sample of collagen I). (Left) Control images of collagen I alone. (Centre) Control images of EuDPA alone.

changes upon exposure of collagen I to EuDPA could also be seen in the Raman bands, indicating structural changes during the fibrillogenesis. The amide I vibration at 1668 cm^{-1} was only detectable at a sufficiently low concentration of EuDPA (0.5 mM), as otherwise the signal was masked by too strong Eu luminescence.

We noticed spectral changes in collagen I even before the fiber could be detected by the naked eye, that is, at lower EuDPA concentrations (below ~2 mM), The strong C—H bending Raman band at 1455 cm^{-1} slightly drifted to 1452 cm^{-1}, and a weak band at 1426 cm^{-1} became more intense and slightly drifted to 1424 cm^{-1}, similar as reported elsewhere [44, 45]. The Raman

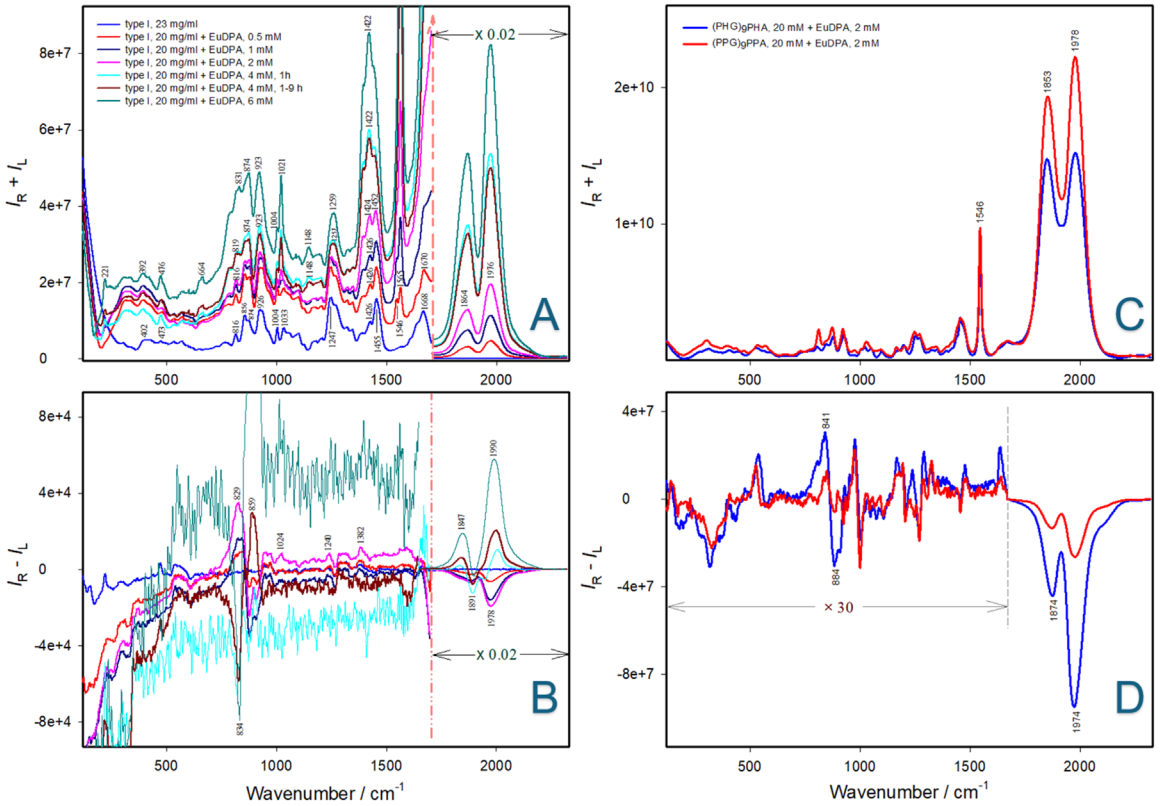

FIGURE 4 | Raman and chiroptical signatures of collagen I and peptide assemblies modulated by EuDPA. (A,B) Raman/luminescence ($I_R + I_L$) and ROA/CPL ($I_R - I_L$) spectra of collagen I alone (control) and in mixtures with the EuDPA complex at the indicated concentrations in 0.1 M acetic acid. (C,D) Corresponding Raman/luminescence ($I_R + I_L$) and ROA/CPL ($I_R - I_L$) spectra of peptide models, $(PHG)_9PHA$ and $(PPG)_9PPA$ (20 mM), mixed with EuDPA (2 mM) in 0.1 M acetic acid. Spectra A, B, and D are shown at a different scale in Figure S6.

band at 1033 cm^{-1} (Phe and Hyp/Pro vibrations) drifted to 1021 cm^{-1} (Figure 4A). Changes in the ROA bands were detected at 1382, 1240, and 1024 cm^{-1} (Figure 4B). Jointly, the spectra indicate changes in the collagen structure upon its chelation to EuDPA.

By further increasing the EuDPA concentration (to ≥4 mM), the strong Eu luminescence prevents detecting any new details in the CPL/ROA spectra of collagen fibers [31], but stronger (or new) Raman bands of collagen I could still be detected (Figure 4A). The most prominent enhancement was encountered for the C—H deformation at 1422 cm^{-1}, amide III vibration at 1257/1259 cm^{-1}, Phe and Hyp/Pro vibrations at 1021 cm^{-1}, C—C stretching at ~810–880 cm^{-1}, and a Raman band of the Hyp ring at 476 cm^{-1} [16]. New bands were detected at 664 and 221 cm^{-1}.

These observations clearly indicate that collagen I conformation is modulated by EuDPA. No changes were recorded in the Raman or ROA spectra when collagen I was titrated by Na_2DPA, indicating that the interaction between collagen and the DPA^{2-} anion alone is extremely weak, and it is indeed the pseudo-D_3 symmetry of EuDPA geometry that is essential to the fibrillogenesis.

The effect of EuDPA was further analyzed by performing a titration at low collagen I concentration (1 mg/mL in 0.1 M acetic acid, Figure S7). At a concentration this low, Raman and ROA signals of collagen alone are almost invisible. Upon chelating EuDPA, the induced CPL patterns started revealing intermolecular interactions between EuDPA and collagen I, thus sampling the structure of collagen itself.

The highest normalized circular intensity difference [CID = $(I_R - I_L) / (I_R + I_L)$] of -3.11×10^{-3} was recorded at the lowest concentrations of EuDPA (0.02 and 0.1 mM). As Eu concentration increases up to ~1 mM, CID value decreases (Figure S8). When the Eu/collagen ratio increases to ~0.5 mmol/g, the "Λ" configuration of EuDPA is no longer dominant, and the collagen fibrils/fibers begin to grow as more Eu is added. Their putative binding to the opposite "Δ" configuration of EuDPA yielded strong CPL, although the absolute CID ratio was smaller than in the fiber-free case (i.e., at lower Eu concentration). Possibly, total luminescence was weakened by the acetic acid and water to a lesser extent at higher Eu concentration. We assume that the Eu-collagen binding is most tight within the range of 1 to 2.5 mmol/g because the induced CPL intensity starts decreasing above ~2.5 mM Eu (Figure S7), and the CID value starts decreasing below ~1 mM Eu (Figure S8).

Unlike in collagen I, where the EuDPA complex induced fibrillogenesis visible to the naked eye, no such effect was encountered in collagen II in wet state. Instead, precipitation or condensation occurred, accompanied by a similar CPL-signal inversion at higher Eu concentrations (Figure S9).

Two collagen-type peptides, $(PHG)_9PHA$ and $(PPG)_9PPA$ exhibited EuDPA-binding characteristics (Figure 4C,D and Figure S6D)

similar to the "clear" (hyaline) fibre-free collagen I encountered at low EuDPA/collagen ratio, indicating that these peptides favor the Λ-EuDPA configuration. Obviously, the binding between Λ-EuDPA and $(PHG)_9PHA$ is slightly tighter, as indicated by a higher CID value. In addition, an induced CPL couplet (± type at 841/884 cm^{-1}) corresponding to the EuDPA $^5D_1 \rightarrow {}^7F_2$ transition was detected in $(PHG)_9PHA$ (Figure 4D), similar as in collagen I before fibrillogenesis started taking place (Figure 4B). Concentration titration of $(PHG)_9PHA$ revealed changes in CID only; binding to the Λ-configuration EuDPA was stable (both in the presence and absence of acetic acid), and unlike in collagen I and II, no inversion of the CPL sign was encountered (Figure S10).

2.3 | Molecular Modelling of Eu-Collagen Interactions

The experimental data established that EuDPA modulates collagen conformation in a concentration- and configuration-dependent manner, with marked differences between collagen I, collagen II, and short collagen-type peptides. To elucidate these effects at a molecular level, we performed MD simulations to probe the lanthanide–peptide interactions and identify possible binding motifs.

As demonstrated elsewhere, MD simulation can provide valuable insights into lanthanide–peptide interactions [33, 42]. Upon binding to $(PHG)_9PHA$, both "Δ" and "Λ" configurations of EuDPA reached a minimum of free energy, at $d \sim 7.6$ and 9.6 Å, respectively. Compared to larger distances (>∼14 Å), the complex of the Δ-form and peptide is energetically different by ∼2 kcal/mol from the Λ-form. However, this is comparable with computational error and should not be compared to experiment in a quantitative way. For $(PPG)_9PPA$ and both enantiomers, the most favored value is larger, $d \sim 11.6$ and 12.2 Å (Figure 5 left). Stable geometries thus obtained (Figure 5, right) indicate a significant role of the —OH group in Hyp, in that it is capable of forming a hydrogen bond with the carboxylic group of the DPA ligand of the EuDPA complex. Nevertheless, no obvious intermolecular hydrogen bonding is captured in the MD snapshots of EuDPA-$(PPG)_9PPA$.

These MD simulations can thus provide a qualitative understanding of the observed data, although the actual binding sites may be more complex, or multiple EuDPA molecules may be involved in peptide binding. The MD data are consistent with ROA/CPL spectra in terms of peptide binding to the EuDPA complex, and Hyp appears to be closer to it than Pro, despite the fact that the interaction of the complex with the collagen-type peptides is rather weak.

In the EuDPA-$(PHG)_9PHA$ model, the complex-peptide distance is greater for the Λ-enantiomer than for the Δ-enantiomer, as consistent with the observed CPL signal. In summary, EuDPA is a racemate containing both enantiomers (Λ and Δ) in solution. At low EuDPA concentrations, collagen I's interaction with EuDPA is loose as no detectable fibrils are formed, and the induced CPL signal is weak. The distance between EuDPA and collagen I is also greater for the Λ-enantiomer, as in the peptide model. In contrast, at high EuDPA concentration, collagen fibrils are formed, and the Δ-enantiomer is encountered in the CPL spectra. Indeed, the very presence of EuDPA-collagen fibrils in wet state (i.e., colocalization of EuDPA and collagen demonstrated in Figure 1) indicates that collagen I and EuDPA do get closer to each other, with the complex possibly linking multiple collagen chains.

3 | Conclusion

We have demonstrated that the EuDPA complex stimulates fibril growth and can serve as a sensitive probe of collagen fibrillogenesis, enabling its direct visualization by simultaneously recording circularly polarized luminescence (CPL) of the complex and Raman scattering of the collagen protein. Supramolecular chirality of collagen and enantioselective binding of the complex are involved.

The EuDPA complex appears to modulate collagen fibrillogenesis through stereospecific interactions. The concentration-dependent induced CPL spectra reveal a dynamic switch in collagen I's enantioselective affinity to EuDPA's Λ- and Δ- configuration. This represents a key advantage over static structural methods such as X-ray crystallography or ensemble-averaging techniques such as NMR spectroscopy.

Molecular dynamics (MD) simulations of the Eu–collagen binding sites in the model peptides support the spectroscopic conclusions. They highlighted the role of the Hyp residues in forming hydrogen bonds with the DPA ligand. MD simulations are consistent with CPL and Raman imaging data, and provide a deeper understanding of the molecular architecture. The complex's pseudo-D_3 symmetry facilitates the collagen-EuDPA interaction by promoting collagen self-assembly at supramolecular level.

The present findings pave the way to designing CPL-based concentration switching materials with predictable chiroptical properties, and to finding alternatives to the not very specific collagen staining commonly used in histology and histopathology. Extracellular matrix could thus be studied more efficiently, and the data also aid the development of biomimetic materials such as the inner lining of artificial (prosthetic) blood vessels.

4 | Experimental Section

Experimental procedures: Collagen I from rat tail tendon (used in Figure 1 and Figure 4) and collagen II from chicken sternal cartilage (used in Figure 2, Figure S3, and Figure S9) were purchased as powder from Sigma-Aldrich and dissolved in 0.1 M acetic acid. Two different stock concentrations were prepared for collagen I (13 and 23 mg/mL), and one for collagen II (25 mg/mL).

Collagen I (1 mg/mL in 0.1 M acetic acid) from calf skin (used in Figure S7) was purchased from Sigma-Aldrich and was used directly in wet state (solution).

Collagen I used in imaging dry-state samples (Figure 2, Figure 3, and Figure S3) was isolated from rat tail tendon at the Institute of Organic Chemistry and Biochemistry and kept as a 4 mg/mL stock in 0.1 M acetic acid.

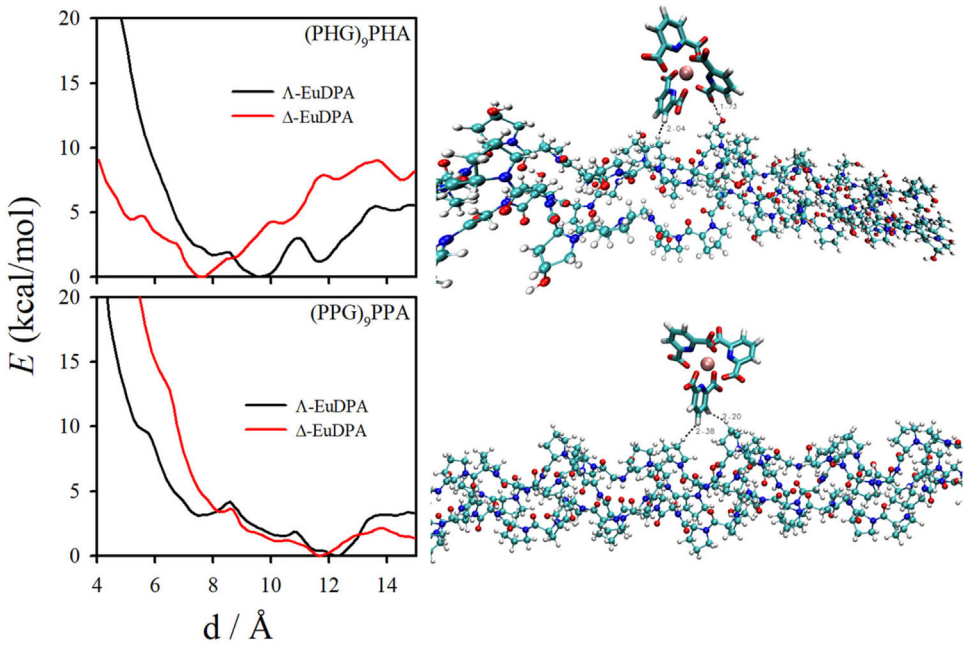

FIGURE 5 | Molecular dynamics (MD) simulation of the binding between EuDPA and two collagen peptides, $(PHG)_9PHA$ and $(PPG)_9PPA$. (Left) Dependence of the free energy (E) on the EuDPA–peptide distance as obtained by the WHAM method. (Right) Snapshots representing the equilibrium geometries of the EuDPA–$(PHG)_9PHA$ (top) and EuDPA–$(PPG)_9PPA$ (bottom) systems. Numbers indicate distances in Ångströms, and the pink ball represents Eu.

Details about collagen-type peptide synthesis are provided in Supporting Information. The europium(III) dipicolinate complex, $Na_3[Eu(DPA)_3]$ (EuDPA), was prepared as described elsewhere [32], and cuvette data (spectra) from all the peptides and proteins were recorded in 0.1 M acetic acid.

Chemical Raman microscopy: The wet-state sample of collagen-EuDPA mixture (Figure 1) was obtained by mixing a 5 µL droplet of collagen I (13 mg/mL in 0.1 M acetic acid) with a 5 µL droplet of EuDPA (8×10^{-3} M in distilled water) directly on a microslide with a preparation needle. The specimen was then covered with a coverslip to obtain a thin enough specimen.

Dry-state *non-triturated* samples of collagen-EuDPA mixtures (Figure 2A–C, and Figure 3) were prepared by mixing a 6 µL droplet of collagen I or II (4 mg/mL in 0.1 M acetic acid) with a 3 µL droplet of EuDPA (1.6×10^{-2} M in distilled water) on a microslide with a preparation needle and letting it dry.

Dry-state *triturated* samples of collagen I and II (Figures 2D–F, and Figure S3) were prepared in the same way, except that mixing was carried out by trituration with a pipette tip in an Eppendorf tube, to achieve greater homogeneity.

Collagen-only (control) dry-state samples (left column in Figure 3 and Figure S3) were prepared by placing a 5 µL droplet of collagen I or II (4 mg/mL in 0.1 M acetic acid) on a microslide and letting it dry. An EuDPA-only sample (middle column in Figure 3) was prepared by placing a 3 µL droplet of EuDPA (1.6×10^{-2} M in distilled water) on a microslide and letting it dry. All dry-state specimens were covered with a coverslip to prevent contamination.

Differential interference contrast (DIC Nomarski) and polarization images were obtained on an Olympus IX81 microscope. Darkfield and positive-type phase-contrast images were obtained on a Zeiss Axio Observer.A1 microscope.

Raman/luminescence images were obtained at room temperature on an upright confocal Raman microscope (WITec alpha300 R) at $\lambda_{exc} = 532$ nm, at spectral integration time 500 ms per pixel, and pixel size between 0.08 and 0.1 µm. Intensity in the spectra was offset to reduce background. The luminescence/Raman images were generated using a spectral window (30–150 cm^{-1} wide) centered at ~2555 cm^{-1} (616 nm) for EuDPA (luminescence signal) and ~2935 cm^{-1} for collagen I/II (Raman scattering signal). The wavenumber and (in case of luminescence) also the corresponding wavelength, rounded to 1 nm, as stated in the spectral images (Figure 1 and Figure 2), denote the centre of the spectral window employed to generate them, using WITec's Project Four software. Background in the images was subtracted based on intensities in front of and behind the relevant peak.

ROA/CPL spectroscopy: ROA/CPL spectra were acquired at room temperature on a BioTools ROA spectrometer (laser excitation 532 nm, resolution 7 cm^{-1}) in a cuvette of ~120 µL volume made of fused silica. The laser power was within the range of 200–1000 mW, and accumulation times were 4 to 72 h. To quench the fluorescence, all biomolecules' samples were irradiated at 200 mW for several hours before measurement, Raman intensities normalized to the water peak at 1650 cm^{-1}, and the remaining fluorescence background was corrected by polynomial baseline. The measurements were carried out at least three times on each sample. The CPL dissymmetry factor g_{lum} value is equivalent to −2CID, where CID (circular intensity difference) is the ROA analogue of the dissymmetry factor, $(I_R - I_L)/(I_R + I_L)$ [30].

5 | Molecular Modelling

To study the Eu-peptide interactions, each of the two peptides, [$(PHG)_9PHA$ [6] and $(PPG)_9PPA$ [46]] was placed in a periodic water box ($120 \times 50 \times 50$ Å) using the Packmol program [47]. The initial system was then minimized using the Amber 18 program suite [48]. The minimized system was then sampled along the Eu-O (peptide) distance, d (4(3)-15 Å), for both enantiomers of the Eu(III) complex (Figure 5). The sampling consisted of 12 $\times$ 1 ns biased runs, with a force constant of 6 kcal·mol^{-1}·Å^{-2}. The weighted histogram analysis method (WHAM) [49] was employed to obtain the dependence of free energy on the distance.

Acknowledgments

The authors are grateful to Dr. Jaroslav Kozák (Institute of Organic Chemistry and Biochemistry, Prague) for kindly providing collagen I isolated at the Department of Biochemical Pharmacology.

Funding

This present study was supported by the Czech Science Foundation (23-05378S to TW and 25–15726S to PB), and the Ministry of Education, Youth and Sports of the Czech Republic through the e-INFRA CZ (ID:90140).

Conflicts of Interest

The authors declare no conflicts of interest.

References

1. C. Wilke, "The Hunt for Proteins in Dinosaur Fossils," *ACS Central Science* 11 (2025): 1020–1023.

2. M. D. Shoulders and R. T. Raines, "Collagen Structure and Stability," *Annual Review of Biochemistry* 78 (2009): 929–958.

3. J. Bella and H. M. Berman, "Crystallographic Evidence for Cα–H···O=C Hydrogen Bonds in a Collagen Triple Helix," *Journal of Molecular Biology* 264 (1996): 734–742.

4. A. Rich and F. H. C. Crick, "The Structure of Collagen," *Nature* 176 (1955): 915–916.

5. G. B. Fields and D. J. Prockop, "Perspectives on the Synthesis and Application of Triple-Helical, Collagen-Model Peptides," *Biopolymers* 40 (1996): 345–357.

6. J. Bella, M. Eaton, B. Brodsky, and H. M. Berman, "Crystal and Molecular Structure of a Collagen-Like Peptide at 1.9 Å Resolution," *Science* 266 (1994): 75–81.

7. J. Roth, C. Hoop, J. K. Williams, V. Nanda, and J. Baum, "Real-time Single-Molecule Observation of Incipient Collagen Fibrillogenesis and Remodeling," *Proceedings of the National Academy of Sciences USA* 121 (2024): e2401133121.

8. M. Akdel, D. E. V. Pires, E. P. Pardo, et al., "A Structural Biology Community Assessment of AlphaFold2 Applications," *Nature Structural & Molecular Biology* 29 (2022): 1056–1067.

9. M. A. B. Kreutzberger, L. T. Yu, T. H. Bui, et al., "A Collagen Triple Helix Without the Superhelical Twist," *ACS Central Science* 11 (2025): 331–345.

10. A. Tampieri, G. Celotti, E. Landi, M. Sandri, N. Roveri, and G. Falini, "Biologically Inspired Synthesis of Bone-Like Composite: Self-Assembled Collagen Fibers/Hydroxyapatite Nanocrystals," Journal of Biomedical Materials Research. Part A 67A (2003): 618–625.

11. J. Brandt, T. N. Krogh, C. H. Jensen, J. K. Frederiksen, and B. Teisner, "Thermal Instability of the Trimeric Structure of the N-Terminal Propeptide of Human Procollagen Type I in Relation to Assay Technology," *Clinical Chemistry* 45 (1999): 47–53.

12. T. A. Shaik, J. L. Lagarto, E. Baria, et al., "Monitoring Changes in Biochemical and Biomechanical Properties of Collagenous Tissues Using Label-Free and Nondestructive Optical Imaging Techniques," *Analytical Chemistry* 93 (2021): 3813–3821.

13. L. Hu, S. Morganti, U. Nguyen, O. R. Benavides, and A. J. Walsh, "Label-Free Optical Imaging of Cell Function and Collagen Structure for Cell-Based Therapies," *Current Opinion in Biomedical Engineering* 25 (2023): 100433.

14. A. C. S. Talari, M. A. G. Martinez, Z. Movasaghi, S. Rehman, and I. U. Rehman, "Advances in Fourier Transform Infrared (FTIR) Spectroscopy of Biological Tissues," *Applied Spectroscopy Reviews* 52 (2017): 456–506.

15. S. Mukherjee, A. Gopinath, B. Madhan, and G. Shanmugam, "Vibrational Circular Dichroism Spectroscopy as a Probe for the Detection of Collagen Fibril and Fibrillation in Solution," *Biosensors and Bioelectronics: X* 10 (2022): 100108.

16. M. G. Martinez, A. J. Bullock, S. MacNeil, and I. U. Rehman, "Characterisation of Structural Changes in Collagen With Raman Spectroscopy," *Applied Spectroscopy Reviews* 54 (2019): 509–542.

17. X. Chen, O. Nadiarynkh, S. Plotnikov, and P. J. Campagnola, "Second Harmonic Generation Microscopy for Quantitative Analysis of Collagen Fibrillar Structure," *Nature Protocols* 7 (2012): 654–669.

18. T. Le, I. Langohr, M. Locker, M. Sturek, and J.-X. Cheng, "Label-Free Molecular Imaging of Atherosclerotic Lesions Using Multimodal Nonlinear Optical Microscopy," *Journal of Biomedical Optics* 12 (2007): 054007.

19. D. Parker, J. D. Fradgley, and K.-L. Wong, "The Design of Responsive Luminescent Lanthanide Probes and Sensors," *Chemical Society Reviews* 50 (2021): 8193–8213.

20. M. C. Heffern, L. M. Matosziuk, and T. J. Meade, "Lanthanide Probes for Bioresponsive Imaging," *Chemical Reviews* 114 (2014): 4496–4539.

21. J. C. G. Bünzli, "Lanthanide Luminescence for Biomedical Analyses and Imaging," *Chemical Reviews* 110 (2010): 2729–2755.

22. K. N. Allen and B. Imperiali, "Lanthanide-Tagged Proteins— An Illuminating Partnership," *Current Opinion in Chemical Biology* 14 (2010): 247–254.

23. J. A. Cotruvo Jr., E. R. Featherston, J. A. Mattocks, J. V. Ho, and T. N. Laremore, "Lanmodulin: A Highly Selective Lanthanide-Binding Protein From a Lanthanide-Utilizing Bacterium," *Journal of the American Chemical Society* 140 (2018): 15056–15061.

24. J. C. Munyemana, X. Sun, L. Li, C. Zhang, E. Qaed, and J. Xiao, "Strategic Enhancement of Collagen Detection Using Lanthanide-Functionalized Collagen Targeted Peptides," *Talanta* 283 (2025): 127170.

25. A. T. Frawley, R. Pal, and D. Parker, "Very Bright, Enantiopure Europium(III) Complexes Allow Time-Gated Chiral Contrast Imaging," *Chemical Communications* 52 (2016): 13349–13352.

26. T. Wu, X. Z. You, and P. Bouř, "Applications of Chiroptical Spectroscopy to Coordination Compounds," *Coordination Chemistry Reviews* 284 (2015): 1–18.

27. M. Cei and F. Zinna, "CPL Photoscopy: Circularly Polarized Luminescence Detected by Chromaticity Differences," *Chemical Science* 16 (2025): 15347–15354.

28. T. Wu, J. Kapitán, V. Mašek, and P. Bouř, "Detection of Circularly Polarized Luminescence of a Cs-Eu III Complex in Raman Optical Activity Experiments," *Angewandte Chemie International Edition* 54 (2015): 14933–14936.

29. T. Wu, J. Kapitán, V. Andrushchenko, and P. Bouř, "Identification of Lanthanide(III) Luminophores in Magnetic Circularly Polarized Luminescence Using Raman Optical Activity Instrumentation," *Analytical Chemistry* 89 (2017): 5043–5049.

30. T. Wu, "A Raman Optical Activity Spectrometer Can Sensitively Detect Lanthanide Circularly Polarized Luminescence," *Physical Chemistry Chemical Physics* 24 (2022): 15672–15686.

31. T. Wu, P. Bouř, T. Fujisawa, and M. Unno, "Molecular Vibrations in Chiral Europium Complexes Revealed by Near-Infrared Raman Optical Activity," *Advanced Science* 11 (2024): 2305521.

32. T. Wu, J. Kessler, and P. Bouř, "Chiral Sensing of Amino Acids and Proteins Chelating With Eu III Complexes by Raman Optical Activity Spectroscopy," *Physical Chemistry Chemical Physics* 18 (2016): 23803–23811.

33. T. Wu, J. Kessler, H. Zhao, and Y. Zhao, "Phosphorylation Site of L-Alanyl-L-Glutamine Identified by Raman Optical Activity Spectroscopy," *Spectrochimica Acta Part A: Molecular and Biomolecular Spectroscopy* 320 (2024): 124587.

34. T. Wu, J. Kessler, J. Kaminský, and P. Bouř, "Recognition of Oligosaccharides by Chirality Induced in Europium (III) Compounds," *Chemistry - An Asian Journal* 13 (2018): 3865–3870.

35. T. Wu and P. Bouř, "Specific Circularly Polarized Luminescence of Eu(III), Sm(III), and Er(III) Induced by N-Acetylneuraminic Acid," *Chemical Communications* 54 (2018): 1790–1792.

36. J. Sahoo, T. Wu, B. Klepetářová, J. Valenta, and P. Bouř, "Binuclear Lanthanide(III) Complexes With Chiral Ligands: Dynamic Equilibria in Solution and Binding With Nucleotides Studied by Spectroscopic Methods," *ChemPlusChem* 85 (2020): 694–700.

37. T. Wu, P. Bouř, and V. Andrushchenko, "Europium (III) as a Circularly Polarized Luminescence Probe of DNA Structure," *Scientific Reports* 9 (2019): 1068.

38. Z. Zhao, Y. Shen, F. Hu, and W. Min, "Applications of Vibrational Tags in Biological Imaging by Raman Microscopy," *Analyst* 142 (2017): 4018–4029.

39. K. Dodo, K. Fujita, and M. Sodeoka, "Raman Spectroscopy for Chemical Biology Research," *Journal of the American Chemical Society* 144 (2022): 19651–19667.

40. R. Pelc, V. Mašek, V. Llopis-Torregrosa, P. Bouř, and T. Wu, "Spectral Counterstaining in Luminescence-Enhanced Biological Raman Microscopy," *Chemical Communications* 55 (2019): 8329–8332.

41. H. Yamakoshi, K. Dodo, A. Palonpon, et al., "Alkyne-Tag Raman Imaging for Visualization of Mobile Small Molecules in Live Cells," *Journal of the American Chemical Society* 134 (2012): 20681–20689.

42. E. Brichtová, J. Hudecová, N. Vršková, J. Šebestík, P. Bouř, and T. Wu, "Binding of Lanthanide Complexes to Histidine-Containing Peptides Probed by Raman Optical Activity Spectroscopy," *Chemistry – A European Journal* 24 (2018): 8664–8669.

43. F. Yan, R. A. Copeland, and H. G. Brittain, "Optical Activity Induced in the Terbium(III) and Europium(III) Tris Complexes of Pyridine-2,6-dicarboxylate Through Association With Monoamino- and Diaminocarboxylic Acids," *Inorganic Chemistry* 21 (1982): 1180–1185.

44. L. D. Barron, L. Hecht, E. W. Blanch, and A. F. Bell, "Solution Structure and Dynamics of Biomolecules From Raman Optical Activity," *Progress in Biophysics and Molecular Biology* 73 (2000): 1–49.

45. A. Rygula, K. Majzner, K. M. Marzec, A. Kaczor, M. Pilarczyk, and M. Baranska, "Raman Spectroscopy of Proteins: A Review," *Journal of Raman Spectroscopy* 44 (2013): 1061–1076.

46. R. Berisio, L. Vitagliano, L. Mazzarella, and A. Zagari, "Crystal Structure of the Collagen Triple Helix Model $[(\text{Pro-Pro-Gly})_{10}]_3$," *Protein Science* 11 (2002): 262–270.

47. L. Martínez, R. Andrade, E. G. Birgin, and J. M. Martínez, "PACKMOL: A Package for Building Initial Configurations for Molecular Dynamics Simulations," *Journal of Computational Chemistry* 30 (2009): 2157–2164.

48. D. A. Pearlman, D. A. Case, J. W. Caldwell, et al., "AMBER, a Package of Computer Programs for Applying Molecular Mechanics, Normal Mode Analysis, Molecular Dynamics and Free Energy Calculations to Simulate the Structural and Energetic Properties of Molecules," *Computer Physics Communications* 91 (1995): 1–41.

49. B. Roux, "The Calculation of the Potential of Mean Force Using Computer Simulations," *Computer Physics Communications* 91 (1995): 275–282.

Supporting Information

Additional supporting information can be found online in the Supporting Information section.

Supporting File 1: agt270293-sup-0001-SuppMat.docx.